THE JOURNAL OF PHYSICAL CHEMISTRY LETTERS
A JOURNAL OF THE AMERICAN CHEMICAL SOCIETY

pubs.acs.org/JPCL

Letter

Manipulating Photogalvanic Effects in Two-Dimensional Multiferroic Breathing Kagome Materials

Haonan Wang and Li Yang*

Cite This: J. Phys. Chem. Lett. 2024, 15, 8689−8696

Read Online

ACCESS | Metrics & More | Article Recommendations | Supporting Information

ABSTRACT: Multiferroic materials, known for their multiple tunable orders, present an exceptional opportunity to manipulate nonlinear optical responses that are sensitive to symmetry. In this study, we propose leveraging electric and magnetic fields to selectively control and switch specific types of photogalvanic effects in two-dimensional multiferroic breathing kagome materials. Taking monolayer Nb_3I_8 as an example, we demonstrate that the shift current, characterized by the real-space shift of electrons and holes, is predominantly unaffected by magnetic order. In contrast, injection current, featured by quantum metric dipole in momentum space, is closely related to valley polarization, which can be controlled by a magnetic field. Furthermore, both photocurrents can be reversed by an out-of-plane electric field via lattice breathing. Our findings reveal the potential of multiferroic breathing kagome structures for multifunctional optoelectronic applications and sensors.

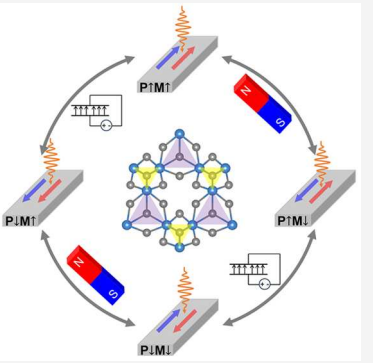

INTRODUCTION

Under optical irradiation, insulating materials with inversion symmetry breaking[1−3] can generate a DC photocurrent via second-order light−matter interactions. This includes the presence of shift current[4−7] and injection current,[8−10] commonly referred to as the photogalvanic effect or bulk photovoltaic effect. These two phenomena originate from the real-space displacement of wave packets and the velocity injection of electrons and holes, respectively.[2,11,12] Recently, numerous novel photogalvanic processes have emerged in quantum materials with specific symmetries, such as the magnetic bulk photovoltaic effect,[9,10,13−15] nonlinear anomalous Hall effect,[16] quantized circular photogalvanic effect,[17] and spin photocurrent.[18−23] Most of these effects have been observed in parity-time-symmetric (PT) antiferromagnetic insulators[9,10,14,15,19] as well as noncentrosymmetric ferroelectric semiconductors[16,20,23] and Weyl semimetals.[17,24−30] These novel photogalvanic effects are deeply rooted in the quantum geometry of electron wave functions, such as quantum metric and Berry curvature,[24,31,32] providing a promising tool to detect emerging quantum phases.

In addition to the generation of various photogalvanic effects, tuning them in a controllable way is also highly desirable. Multiferroic materials appear to be ideal candidates for such manipulations, given their switchable multiferroic orders are interconnected via specific symmetries. For instance, recent proposals have been made to manipulate injection current in stacking-induced multiferroic bilayers.[13] However, the manipulation of the shift current is constrained by symmetry limitations. Therefore, it is crucial to explore switchable injection and shift currents in two-dimensional (2D) multiferroic materials, despite only a limited number of 2D multiferroic materials having been predicted over the past decade.[33−37]

In this work, we propose to selectively manipulate both injection and shift currents in a family of 2D breathing kagome materials: Ta_3X_8 (X = Br, I) and Nb_3X_8 (X = Cl, Br, I). These materials have aroused significant research interest as a promising platform for topological flat bands,[38] intrinsic anomalous valley Hall effect,[39] Mott insulator,[40] and multiferroics.[41−44] Using first-principles calculations, we demonstrate that the unique lattice breathing allows for the selective tuning and switching of injection and shift currents through electric and magnetic fields. For instance, in monolayer Nb_3I_8, we find that the valley polarization, which causes an asymmetric distribution of quantum metric dipole in momentum space, can couple with both the out-of-plane ferromagnetic (FM) order and ferroelectric (FE) order. Consequently, when the magnetic order or electric polarization is reversed, the direction of the injection current also reverses. Conversely, shift current only depends on the in-plane lattice breathing instead of valley polarization. As a result, we predict the presence of four distinct nonlinear optical responses corresponding to different multiferroic configurations, provid-

Received: June 21, 2024
Revised: August 3, 2024
Accepted: August 15, 2024
Published: August 19, 2024

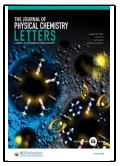

https://doi.org/10.1021/acs.jpclett.4c01844
J. Phys. Chem. Lett. 2024, 15, 8689−8696

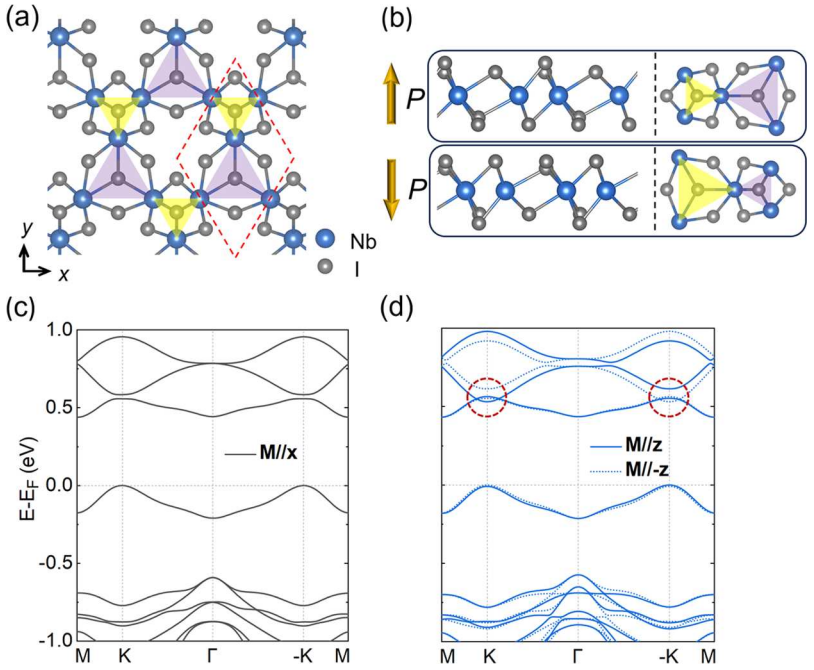

Figure 1. (a, b) Top view and side view of atomic structure of the breathing kagome lattice Nb_3I_8 monolayer. The purple and yellow shaded regions represent two kinds of Nb trimers with different bond length. The two ferroelectric phases with opposite out-of-plane polarization can be switched through a lattice breathing that space inversion. (c) Band structure of Nb_3I_8 monolayer with $\boldsymbol{M}\|\boldsymbol{x}$, (d) Band structures for $\boldsymbol{M} \parallel \boldsymbol{z}$ (blue solid line) and $\boldsymbol{M}\|-\boldsymbol{z}$ (blue dotted line). Energy bands at $\boldsymbol{k}$ and $-\boldsymbol{k}$ are symmetrical for $\boldsymbol{M}\|\boldsymbol{x}$, while they are asymmetrical for $\boldsymbol{M}\|\boldsymbol{z}$, referred to as valley polarization. Bands in the dashed circles contribute to the first peak of optical interband transitions. All bands are reversed between $\boldsymbol{k}$ and $-\boldsymbol{k}$ for $\boldsymbol{M}\|-\boldsymbol{z}$ due to time reversal.

ing a method for selectively manipulating nonlinear photocurrents in a 2D breathing kagome lattice.

RESULTS AND DISCUSSION

The general form of second-order DC photocurrent can be written as

$$J^a = \chi^a_{bc}(0;\ \omega,\ -\omega)E_b(\omega)E_c(-\omega) \tag{1}$$

where the subscripts b and c denote the polarization directions of electric field (E) of incident light, and the superscript a refers to the photocurrent direction in Cartesian coordinates. For insulators, the photoresponsivity $\chi^a_{bc}\ (0;\ \omega,\ -\omega)$ is mainly contributed from interband excitations, including shift current and injection current.[2] Under linearly polarized light, through the quantum perturbation theory within the independent particle approximation, the photoconductivity tensors of shift (σ^a_{bc}) and injection (η^a_{bc}) currents in the length gauge can be expressed as[2,9,10]

$$\sigma^a_{bc}(0;\ \omega,\ -\omega) = -\frac{i\pi e^3}{\hbar^2}\sum_{m,n}\int\frac{\mathrm{d}\mathbf{k}}{(2\pi)^2}\{r^b_{mn},\ r^{c;a}_{mn}\}\delta(\omega-\omega_{mn}) \tag{2}$$

$$\eta^a_{bc}(0;\ \omega,\ -\omega) = -\frac{\pi e^3}{\hbar^2}\sum_{m,n}\int\frac{\mathrm{d}\mathbf{k}}{(2\pi)^2}\Delta^a_{mn}\{r^b_{mn},\ r^c_{mn}\}\tau\delta(\omega-\omega_{mn}) \tag{3}$$

where $r^b_{mn} = \frac{v^b_{mn}}{i\omega_{mn}}$ is the interband dipole matrix element between the conduction band m and valence band n. $\{r^b_{mn},r^{c;a}_{nm}\}$ in eq 2 is defined as $(r^b_{mn}r^{c;a}_{nm} + r^c_{mn}r^{b;a}_{nm})$. $r^{c;a}_{nm} = \frac{\partial r^c_{nm}}{\partial k^a} - i(\mathcal{A}^a_{nn} - \mathcal{A}^a_{mm})r^c_{nm}$ is the generalized derivative with respect to the crystal momentum k, where $\mathcal{A}^a_{mm}$ is the Berry connection matrix element. $\{r^b_{mn},r^c_{mn}\}$ is the Hermitian metric tensor defined as $r^b_{mn}r^c_{mn} + r^b_{nm}r^c_{nm}$. Such Hermitian metric which involves optical transition dipoles is distinct from the Fubini-Study metric in the quantum geometric tensor relevant to the nonlinear Hall effect.[45] $\Delta^a_{mn} = v^a_{mm} - v^a_{nn}$ denotes the group velocity difference where v^a_{mm} stands for the velocity matrix element. The integrand of injection current $\Delta^a_{mn}\{r^b_{mn}r^c_{mn}\}$ in eq 3 is termed as quantum metric dipole.[46] τ denotes the carrier lifetime and is set to 0.1 ps in our calculations (see SI). Both shift current and injection current are rooted in quantum geometry of electron wave functions.[24,31]

It is noteworthy that injection current and shift current have essentially distinct parities under spatial inversion and time reversal operations.[24] Under time-reversal transformation $\mathcal{T}$, $\mathrm{Tr}^a_{mn}(\mathbf{k}) = r^a_{nm}(-\mathbf{k})$, and the Berry connection is even, namely, $\mathcal{T}\mathcal{A}^b_{mm}(\mathbf{k}) = \mathcal{A}^b_{mm}(-\mathbf{k})$. Hence, both terms $\{r^b_{mn}r^c_{mn}\}$ and $\{r^b_{mn},r^{c;a}_{nm}\}$ are even in the momentum space. Therefore, according to eq 2, shift current is immune to time-reversal operation $\mathcal{T}$. On the other hand, the group velocity difference Δ^a_{mn} in eq 3 is odd in momentum space because $\mathcal{T}v^a_{mm}(\mathbf{k}) = -v^{*a}_{mm}(-\mathbf{k}) = -v^a_{mm}(-\mathbf{k})$. Thus, injection current is odd under $\mathcal{T}$. Under spatial inversion transformation $\mathcal{P}$, denoted by $\mathcal{P}v^a_{mn}(\mathbf{k}) = -v^a_{mn}(-\mathbf{k})$, $\mathcal{P}r^a_{mn}(\mathbf{k}) = -r^a_{mn}(-\mathbf{k})$, and $\mathcal{P}r^{b;a}_{nm}(\mathbf{k}) = r^{b;a}_{nm}(-\mathbf{k})$. Consequently, both injection and shift currents reverse their directions by the inversion operation $\mathcal{P}$. Based on the above symmetry analysis, the spatial inversion associated with FE polarization switching and time reversal associated with magnetic order switching can be employed to selectively control injection and shift currents, respectively, in multiferroic materials.

Monolayer Kagome Nb_3I_8. To demonstrate this idea, a material with both controllable parity and time reversal symmetries is required, bringing our attention to a family of emerging 2D kagome materials, niobium halide semiconduc-

https://doi.org/10.1021/acs.jpclett.4c01844
J. Phys. Chem. Lett. 2024, 15, 8689−8696

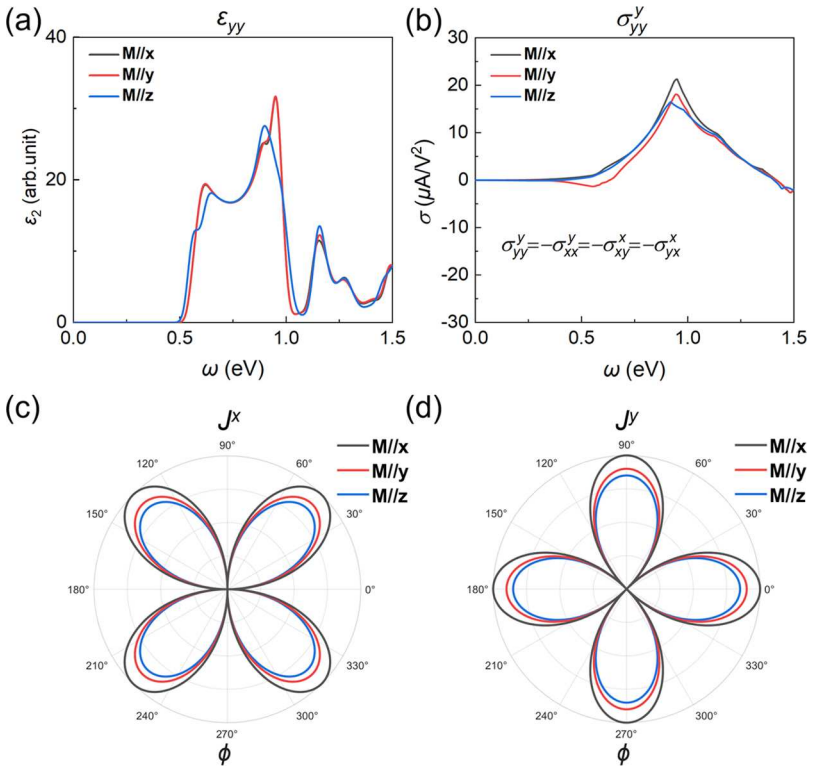

Figure 2. Optical responses in Nb_3I_8 monolayer with varying magnetic orders. (a) Imaginary part of linear optical responses ϵ_{yy}. (b) Shift current photoconductivity of σ^y_{yy} component, other nonvanishing components reverse sign due to the 3-fold rotational symmetry. All varying magnetic orders have same nonvanishing components. (c, d) Angle-dependent shift current (J^x, J^y) at photon energy of 0.9 eV. Angular coordinate ϕ denotes the angle between the x-axis and incident light polarization direction, and radial coordinate stands for amplitude of photocurrents. The maximum amplitude of shift current (J^x, J^y) for $\boldsymbol{M}\|\boldsymbol{z}$ is comparable to that for $\boldsymbol{M}\|\boldsymbol{x}$ and $\boldsymbol{M}\|\boldsymbol{y}$.

tors, which have attracted significant research interest because of their unique multiferroic character and topological properties. Here we choose monolayer Nb_3I_8 as an example, which has a space group of $P3m1$. As shown in Figure 1a,b, the atomic structure has a 3-fold in-plane rotational symmetry (C_{3v}) and a mirror symmetry with respect to the yz mirror plane (M_x). Three Nb ions are trimerized as a Nb_3 cluster in the unit cell. Two types of Nb_3 trimers with different bond lengths form a distorted Kagome lattice that breaks the inversion symmetry, leading to an out-of-plane polarization.[41,42] Interestingly, the out-of-plane polarization is inherently coupled with lattice breathing. As a result, FE polarization switching by a vertical electric field is also accompanied by the in-plane inversion of the atomic configuration. Finally, 1 μ_B magnetic moment for each Nb_3 trimer has been calculated, consistent with previous results.[39,47] Hence, the FE/FM orders in monolayer Nb_3I_8 can be switched via $\mathcal{P}/\mathcal{T}$ symmetry operation.

The electronic band structures of monolayer Nb_3I_8 are plotted in Figure 1c,d. When the spin orientation is along the in-plane x-axis ($\mathbf{M}\|\mathbf{x}$), the energy bands are symmetric in Figure 1c. When the spin orientation aligns along the out-of-plane z-axis ($\mathbf{M}\|\mathbf{z}$), the band structure presents an energy asymmetry at $\mathbf{k}$ and $-\mathbf{k}$, resulting in a valley polarization. As shown in circled areas, the energy difference between the bottoms of the second conduction band at $\mathbf{k} = \mathbf{K}$ and $\mathbf{k} = -\mathbf{K}$ is around 80 meV, which can quantitatively describe the valley polarization. Notably, the valley polarization is reversed between $\mathbf{k}$ and $-\mathbf{k}$ points when the out-of-plane spin orientation is flipped ($\mathbf{M}\|-\mathbf{z}$) in Figure. 1d because the spin flipping is achieved through time reversal.

Linear Optical Response. Figure 2a exhibits a broad linear optical response profile. Optical transitions between the top valence band and bottom conduction band are forbidden because of their opposite spins,[39] and the allowed lowest-energy transition occurs between the top valence band and the second lowest-energy conduction band around the valleys, $\mathbf{k} = \mathbf{K}$ and $\mathbf{k} = -\mathbf{K}$, at an energy of 0.6 eV. The linear optical spectra (the imaginary part of ε_{yy}) with different spin orientations ($\mathbf{M}\|\mathbf{x}$, $\mathbf{M}\|\mathbf{y}$, and $\mathbf{M}\|\mathbf{z}$) are also plotted, which are not sensitive to the spin orientation. Moreover, we also find that they are degenerate for two FE phases because the linear response is even under $\mathcal{P}$.[2]

Shift Current. Because of the second-order nature of the photogalvanic effect, it is crucial to identify the nonzero independent components of the photoconductivity tensor. We note that in our investigations presented below, we only focus on the photoinduced charge current with in-plane components. The photoconductivities are calculated by eqs 2 and 3 via summation across all bands regardless of spins. As analyzed above, the shift current is immune to time reversal. Therefore, its independent components are only constrained by the space group symmetry, i.e., the mirror symmetry M_x and rotational symmetry C_{3v}. Because the dipole matrix element r^a_{mn} is a polar vector in momentum space, r^x_{mn} is odd and r^y_{mn} is even with respect to the M_x mirror plane. In consequence, all the nonvanishing tensor components are constrained to $\sigma^y_{yy} = -\sigma^y_{xx} = -\sigma^x_{xy} = -\sigma^x_{yx}$, and we only analyze one component, *e.g.*, σ^y_{yy}, in Figure 2b.

https://doi.org/10.1021/acs.jpclett.4c01844
J. Phys. Chem. Lett. 2024, 15, 8689−8696

First, significant shift current is observed. The magnitude of σ^y_{yy} reaches 22 μA/V^2. This is larger than that (~8 μA/V^2) of monolayer MoS_2[48] and closed to that (~28 μA/V^2) of sliding-induced multiferroic bilayer VS_2.[13] It is noteworthy that the magnitude has been multiplied by an effective thickness (~4.1 Å) to facilitate comparisons with the bulk photovoltaic effect in 3D bulk materials. Second, as expected, the shift current is not sensitive to the spin orientation. In Figure 2b, the shift current spectrum is nearly identical with different spin orientations (**M**||**x**, **M**||**y**, and **M**||**z**), where the minor changes are owing to the variation of band structures.

Furthermore, we have calculated the shift current with respect to the polarization direction of incident light, which can be directly measured in experiment. We consider only the direction of the incident light along the out-of-plane direction in the whole work. This is because the depolarization effect via the electron−hole exchange interaction will quench the out-of-plane electric field of light and subsequent optical response.[49] For light with an in-plane polarization direction, its optical field is $|E_0|e^{-i\omega t}(\cos\phi, \sin\phi)$ + c.c. The in-plane shift current can be calculated as $(J^x, J^y) = |E_0|\sigma^y_{yy}(-\sin 2\phi, \cos 2\phi)$ and is plotted in Figures 2c and d, respectively. In Figure 2c, the shift current along the x direction (J^x) reaches its maximum amplitude when the light is polarized at the 45° angle to the current direction. On the other hand, for shift current along the y direction (J^y) plotted in Figure. 2d, it attains the peak value when the light is polarized either along or perpendicular to the current direction. Finally, in line with the findings in Figure. 2b, all these shift currents exhibit low sensitivity to the spin orientation.

Injection Current. Unlike the shift current, the injection current is highly dependent on the spin orientation. For **M**||**x**, the symmetry operation is M_x. According to eq 3, because the velocity matrix element v^x_{mm} behaves as a polar vector in momentum space, Δ^x_{mm} is odd and Δ^y_{mm} is even with respect to the $yz(M_x)$ mirror plane. Hence, there are three independent nonzero components, η^y_{yy}, η^y_{xx}, and $\eta^x_{xy} = \eta^x_{yx}$. For **M**||**y**, the symmetry operation is M_xT. $\{r^b_{mn}, r^c_{mn}\}$ is even for $b = c$, and odd for $b \neq c$ under the combined $M_x\mathcal{T}$ symmetry. Meanwhile, the group velocity difference Δ^x_{mn} is even, and Δ^y_{mn} is odd under $M_x\mathcal{T}$. Therefore, there are three independent components: η^x_{xx}, η^x_{yy}, and $\eta^y_{xy} = \eta^y_{yx}$. For **M**||**z**, the symmetry operations are $M_x\mathcal{T}$ and C_{3v} that enforce only one independent component to survive, $\eta^x_{xx} = -\eta^x_{yy} = -\eta^y_{xy} = -\eta^y_{yx}$. Essentially, the number of these nonzero components for different spin orientations is constrained by their distinct magnetic point groups, as summarized in Table 1. In the following section, we focus on the η^x_{yy} component as an example. The results of other components are presented in the Supporting Information.

Table 1. Magnetic Point Group, Nonzero Shift Current, and Injection Current Components for Various Magnetization Directions M||x, M||y and M||z[a]

	magnetic point group	shift current component	injection current component
M||**x**	2′	$-\sigma^y_{yy} = \sigma^y_{xx} = \sigma^x_{xy} = \sigma^x_{yx}$	η^y_{yy}, η^y_{xx}, $\eta^x_{xy} = \eta^x_{yx}$
M||**y**	2		η^x_{xx}, η^x_{yy}, $\eta^y_{xy} = \eta^y_{yx}$
M||**z**	−3m′		$-\eta^x_{xx} = \eta^x_{yy} = \eta^y_{xy} = \eta^y_{yx}$

[a]The nonzero shift current and injection current components are constrained by symmetry.

Figure 3a plots the spectra of the η^x_{yy} component with different spin orientations. Overall, an enhanced response of injection current is observed. For **M**||**z**, the first peak at an incident light energy of 0.6 eV reaches ~100 μA/V^2, larger than that in sliding-induced multiferroic VS_2 bilayer (~10 μA/V^2)[13] and MoS_2 monolayer (~100 μA/V^2).[50]

Importantly, the injection current is highly sensitive to the spin orientations. We focus on the absorption edge region, which is the shadow area in Figure 3a. The first peak of η^x_{yy} reaches its maximum (~100 μA/V^2) when **M**||**z**. Then it begins to decrease as the spin orientation rotates into the in-plane direction. When the spin orientation is along the in-plane y direction, the magnitude decreases to 12 μA/V^2. Finally, when **M**||−**z**, the magnitude of η^x_{yy} reaches the maximum again but with an opposite sign. We note that η^x_{yy} becomes zero when **M**||**x** because of the symmetry constrain.

Based on eq 1 and symmetries of the injection current tensors, the in-plane injection current components J^x and J^y are plotted in Figure 3b and c, respectively. Consisting with the result of the η^x_{yy} component, the injection current is significantly larger for the out-of-plane spin orientation and substantially reduced for the in-plane spin orientation. In the case of **M**||**z**, the injection current along the x direction (J^x) reaches its maximum amplitude when the incident light is polarized either along or perpendicular to the current direction. While for the injection current along the y direction (J^y) plotted in Figure 3c, it attains the peak value when the incident light is polarized at an angle of 45° to the current direction. Compared with the results of shift current in Figure 2c,d, the angle dependence of both current components is inversed in injection current. It is noteworthy that when the in-plane incident light is parallel or perpendicular to the spin orientation, the in-plane injection current is larger in directions perpendicular to the in-plane spin orientation, namely, J^x for **M**||**y** is larger than that for **M**||**x**, and vice versa, for J^y, this phenomenon has also been observed in previous research.[13]

To better address this characteristic of injection current, we have plotted the variation of the peak value of injection current with respect to spin orientation in Figure 3d. It is clearly seen that both injection current components significantly vary with the spin orientation and can switch the direction by flipping spins. Moreover, we find that the amplitude and direction of injection current are strongly correlated to the valley polarization. A large valley polarization accompanies with a large injection current, indicating that the valley-polarization induced asymmetric band structure (Figure 1d) plays an important role in determining the amplitude of injection current.

To elucidate the underlying mechanism of spin dependence, we analyze the distribution of group velocity difference and quantum metric dipole in momentum space at the photon energy of 0.6 eV for **M**||**y** and **M**||**z**, corresponding to the interband transitions around **k** = **K** and **k** = −**K** in reciprocal space, as marked by the circles in Figure 1d. According to eq 3, the injection current photoconductivity η^x_{yy} is the integral of the quantum metric dipole that is the absorption rate $|r^y_{mn}|^2\delta(\omega - \omega_{mn})$ weighted by group velocity difference Δ^x_{mn}. First, although the distribution of the absorption rate $|r^y_{mn}|^2\delta(\omega - \omega_{mn})$ for **M**||**y** is more symmetric than that for **M**||**z** around **k** = **K** and **k** = −**K** points (see Supporting Information), their integral that gives rise to the linear optical response (the imaginary part of ε_{yy}) is nearly identical, as shown in Figure 2a. Hence, the main difference in the nonlinear response for **M**||**y** and **M**||**z** comes

https://doi.org/10.1021/acs.jpclett.4c01844
J. Phys. Chem. Lett. 2024, 15, 8689−8696

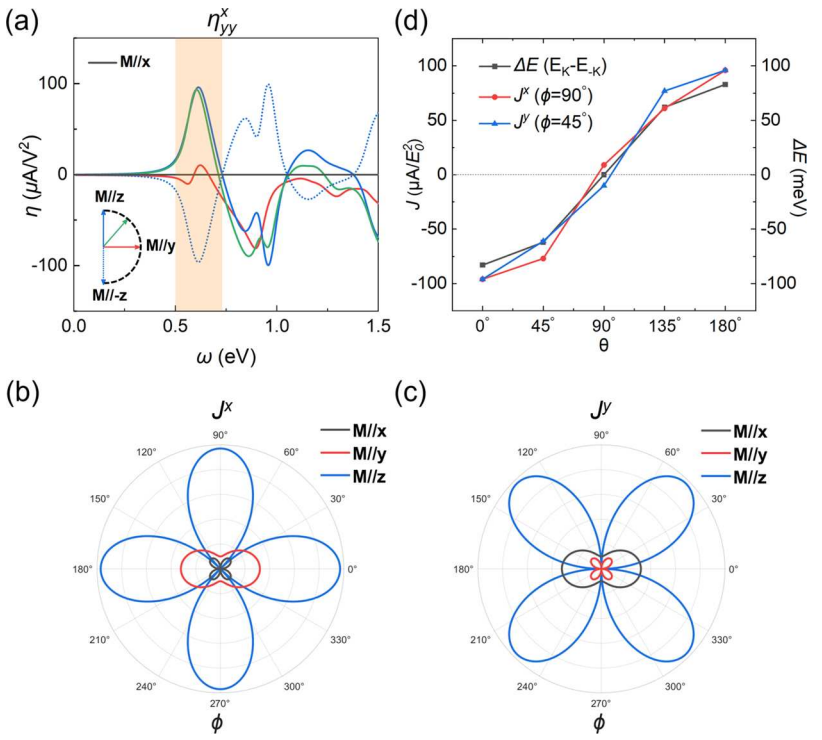

Figure 3. Injection current in Nb_3I_8 monolayer with varying magnetic orders. (a) Injection current photoconductivity of η^x_{yy} component with varying magnetic orders. The shaded region presents the peak enhanced by the out-of-plane magnetic order. All components reverse as spin flips from $M\|z$ to $M\|-z$. (b, c) Angle-dependent injection current (J^x, J^y) at photon energy of 0.6 eV. Angular coordinate ϕ denotes the angle between the x-axis and incident light polarization direction, and radial coordinate stands for amplitude of photocurrents. The maximum amplitude of injection current for $M\|z$ is significantly greater than that for $M\|x$ and $M\|y$. (d) Injection current (J^x, J^y) and energy difference between $k = K$ and $k = -K$ points for the bottom conduction band as a function of θ, where θ denotes the polar angle between the out-of-plane z-axis and spin orientation. The current is in unit of $\mu A/E_0^2$, where E_0 denotes amplitude of the incident light field.

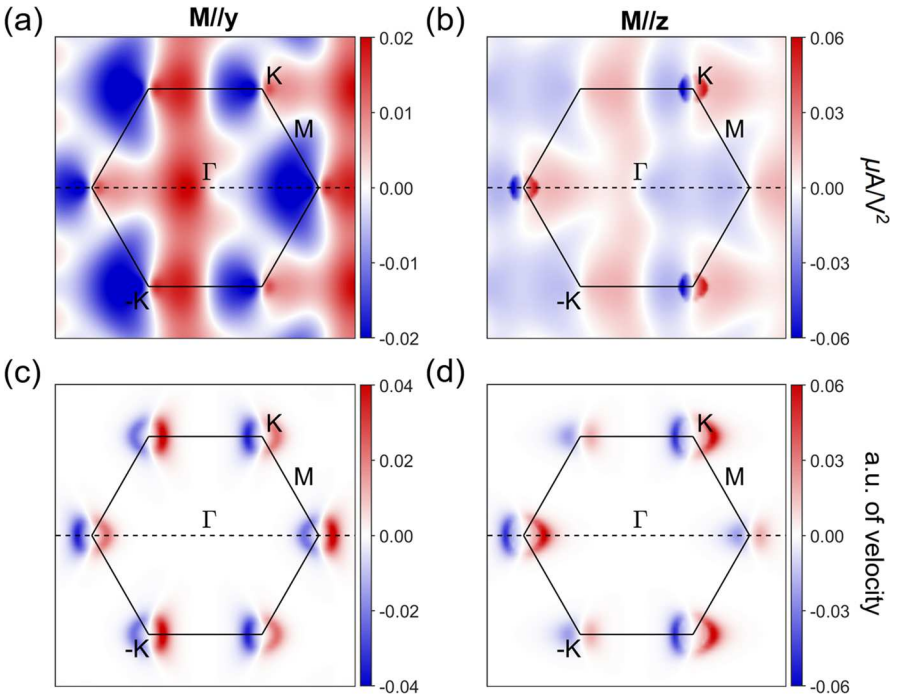

Figure 4. (a, b) Distributions of group velocity difference Δ^x_{mn} between the top valence band and bottom conduction band in momentum space with **M**||**y** and **M**||**z**, respectively. (c, d) Distributions of quantum metric dipole tensor $\Delta^x_{mn}|r^y_{mn}|^2$ at photon energy of 0.6 eV in momentum space with **M**||**y** and **M**||**z**, respectively.

from the group velocity difference Δ^x_{mn}. The distributions of group velocity difference Δ^x_{mn} between the top valence band and bottom conduction band are plotted as Figure 4a and b for **M**||**y** and **M**||**z**, respectively. Since both magnetic config-

https://doi.org/10.1021/acs.jpclett.4c01844
J. Phys. Chem. Lett. 2024, 15, 8689−8696

Table 2. Properties of Shift and Injection Current for Typical Two-Dimensional Multiferroic Materials[a]

	symmetry operation for FE switching	NLO response	parity under FE switching	parity under FM switching	# of values
multiferroic sliding systems[13]	$M_z\mathcal{T}$	shift	×	×	2
		injection	√	√	
multiferroic breathing kagome lattice	$\mathcal{P}$	shift	√	×	4
		injection	√	√	

[a]The symbols, √ and ×, denote whether the photocurrent will reverse or retain its direction upon ferroelectric (FE) or ferromagnetic (FM) switching. The final column indicates the number of different nonlinear photocurrent values corresponding to FE/FM switching.

urations preserve the $M_x\mathcal{T}$ symmetry, Δ^x_{mn} is symmetric with respect to the xz mirror plane (M_y), while it is asymmetric with respect to the yz mirror plane (M_x). Therefore, the quantum metric dipole $\Delta^x_{mn}|r^y_{mn}|^2$ is nonvanishing that gives rise to a net current of η^x_{yy}.

Moreover, for $\mathbf{M}\|\mathbf{z}$ plotted in Figure 4b, Δ^x_{mn} exhibits greater asymmetry at $\mathbf{k} = \mathbf{K}$ and $\mathbf{k} = -\mathbf{K}$ points. This agrees with its larger valley polarization, which induces energy and group velocity asymmetry in momentum space (see Figure 1d) and thereby enhances current injection. Conversely, in the case of in-plane magnetic orders, the valley polarization diminishes, allowing energy and group velocity symmetry to persist and suppressing the current injection. In consequence, the quantum metric dipole exhibits a more asymmetric distribution when $\mathbf{M}\|\mathbf{z}$, as illustrated in Figure 4c,d, contributing to a larger integral value. This analysis demonstrates that the injection current originates from the asymmetry of quantum metric dipole in momentum space and strongly indicates that the injection current can be amplified by valley polarization. The fact that the injection current is enhanced when the magnetization vector is aligned along the out-of-plane direction has also been observed in $MnPSe_3$ monolayer.[15]

Selectively Tunable Nonlinear Photocurrent. Table 2 summarizes the properties of shift and injection currents in multiferroic 2D kagome materials and compares them with those of sliding multiferroic bilayers.[13] In sliding multiferroic bilayers, although injection current can be reversed by FE or FM switching, the shift current remains unaffected because of the protection of the horizontal mirror symmetry. On the other hand, in 2D breathing kagome lattices, the two FE phases are interrelated through $\mathcal{P}$, that can reverse both the injection and shift currents.[24] Furthermore, reversing the spin orientation in 2D kagome lattices leads to a reversal of the injection current, while the shift current remains unaffected. In Supporting Information, we have plotted the real-space spin and charge distributions of the conduction band minimum (CBM) and valence band maximum (VBM) and presented a detailed analysis of the relation between them and photocurrents under the P/T symmetries.

This offers a unique tuning knob for separately controlling shift and injection photocurrents. Figure 5 illustrates the four possible multiferroic phases: **P↑M↑**, **P↑M↓**, **P↓M↓**, and **P↓M↑**, where the up/down arrows represent the out-of-plane direction of the FE or FM order. The injection current can be solely reversed by switching the magnetic field, while the shift current can be solely reversed by switching both electric and magnetic fields. By applying an appropriate external field, we can selectively switch the specific type of DC photocurrent. Additionally, due to the different spectra and amplitudes of shift and injection currents, the four multiferroic phases exhibit different overall photocurrents, resulting in four-stage photocurrent states. This provides a novel approach to identifying

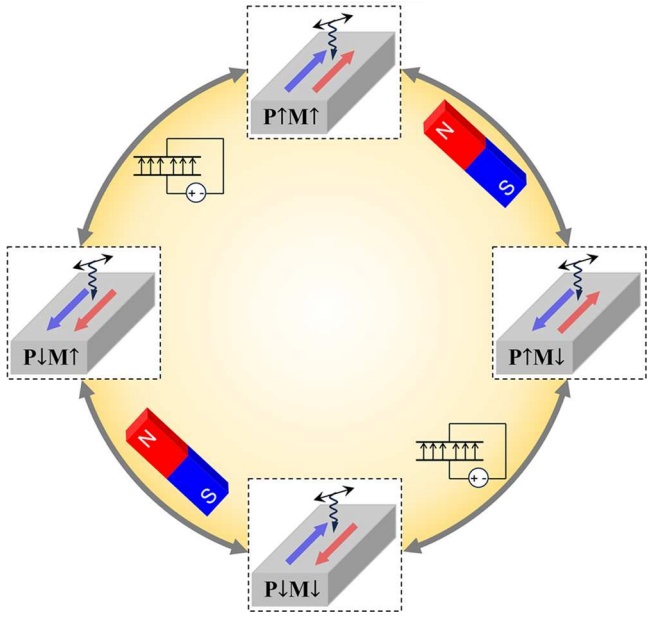

Figure 5. Schematic plot of multiferroic phases and corresponding nonlinear photocurrent in breathing kagome lattice Nb_3I_8 monolayer. The four distinct phases are denoted as **P↑M↑** (top), **P↑M↓** (right), **P↓M↓** (bottom), and **P↓M↑** (left), respectively. The four multiferroic phases can be switched by applying an external electric field/magnetic field, where the injection current (blue arrow) and shift current (red arrow) are independently reversed.

multiferroic phases and can also serve as multifunctional sensors for detecting both electric and magnetic fields.

In conclusion, the findings about tunable photocurrents, as presented above, remain valid for diverse conditions, including those induced by circularly polarized light and varying Hubbard values, as detailed in Supporting Information. Therefore, our approach to manipulate photocurrent inherently broadens its applicability across a wide range of multiferroic breathing kagome materials. Notably, one such breathing kagome material, Nb_3Cl_8, has been identified as a Mott insulator.[40,51] Investigations of photoinduced effect for Mott insulators extend beyond conventional band theory, necessitating the application of many-body theories such as Floquet dynamical mean-field theory.[52,53]

Unlike typical 2D magnets, the magnetic order in multilayer Nb_3I_8 changes with the layer thickness. For example, bilayer and trilayer Nb_3I_8 exhibit several unique antiferromagnetic ground states.[54] Exploring the bulk photovoltaic effect in multilayer Nb_3I_8 is intriguing due to these variations. However, unlike the ferromagnetic order observed in monolayers, controlling the Néel vector in antiferromagnets presents a known challenge. Consequently, utilizing a magnetic field to modulate the injected current may not be effective in few-layer

https://doi.org/10.1021/acs.jpclett.4c01844
J. Phys. Chem. Lett. 2024, 15, 8689−8696

Nb_3I_8. This underscores the importance of further research to comprehensively investigate layer-dependent bulk photovoltaic conductance.

Additionally, while exploring excitonic effects on nonlinear optical responses is both intriguing and crucial, it poses substantial challenges for theoretical calculations due to the significant increase in the number of Feynman diagrams needed beyond the independent particle approximation.[55] However, this work primarily focuses on field-tunable photocurrents, which arise from material symmetries. Although excitonic effects may alter the details of optical spectra, they do not impact the underlying symmetries. Consequently, our primary conclusion regarding tunable photocurrents remains robust, even when excitonic influences. We also anticipate future research to explore switchable photogalvanic effects with electron−hole interactions included in a broader range of multiferroic materials.

■ ASSOCIATED CONTENT

Supporting Information

The Supporting Information is available free of charge at https://pubs.acs.org/doi/10.1021/acs.jpclett.4c01844.

Computational details; k-point mesh convergence test; Analyses of the photoconductivities of injection current in the monolayer Nb_3I_8; Analyses of absorption rates of the monolayer Nb_3I_8; Hybrid functional calculations of band structures and optical responses for monolayer Nb_3I_8; Band structures and optical responses for U = 3.0 eV; Analyses of shift and injection current under circularly polarized light; Second harmonic generation for monolayer Nb_3I_8 (PDF)

■ AUTHOR INFORMATION

Corresponding Author

Li Yang − *Department of Physics and Department of Physics and Institute of Materials Science and Engineering, Washington University, St. Louis, Missouri 63130, United States;* orcid.org/0000-0002-8611-6359; Email: lyang@physics.wustl.edu

Author

Haonan Wang − *Department of Physics, Washington University, St. Louis, Missouri 63130, United States;* orcid.org/0000-0003-3626-8810

Complete contact information is available at: https://pubs.acs.org/10.1021/acs.jpclett.4c01844

Notes

The authors declare no competing financial interest.

■ ACKNOWLEDGMENTS

H.W. is supported by the National Science Foundation (NSF) DMR-2124934. L.Y. is supported by Designing Materials to Revolutionize and Engineer our Future (DMREF) DMR-2118779. The simulation used Anvil at Purdue University through allocation DMR100005 from the Advanced Cyberinfrastructure Coordination Ecosystem: Services and Support (ACCESS) program, which is supported by National Science Foundation Grant Nos. 2138259, 2138286, 2138307, 2137603, and 2138296.

■ REFERENCES

(1) Aversa, C.; Sipe, J. E. Nonlinear Optical Susceptibilities of Semiconductors: Results with a Length-Gauge Analysis. *Phys. Rev. B* **1995**, *52*, 14636.

(2) Sipe, J. E.; Shkrebtii, A. I. Second-Order Optical Response in Semiconductors. *Phys. Rev. B* **2000**, *61*, 5337.

(3) Parker, D. E.; Morimoto, T.; Orenstein, J.; Moore, J. E. Diagrammatic Approach to Nonlinear Optical Response with Application to Weyl Semimetals. *Phys. Rev. B* **2019**, *99*, No. 045121.

(4) Young, S. M.; Zheng, F.; Rappe, A. M. First-Principles Calculation of the Bulk Photovoltaic Effect in Bismuth Ferrite. *Phys. Rev. Lett.* **2012**, *109*, No. 236601.

(5) Tan, L. Z.; Rappe, A. M. Enhancement of the Bulk Photovoltaic Effect in Topological Insulators. *Phys. Rev. Lett.* **2016**, *116*, No. 237402.

(6) Young, S. M.; Rappe, A. M. First Principles Calculation of the Shift Current Photovoltaic Effect in Ferroelectrics. *Phys. Rev. Lett.* **2012**, *109*, No. 116601.

(7) Rangel, T.; Fregoso, B. M.; Mendoza, B. S.; Morimoto, T.; Moore, J. E.; Neaton, J. B. Large Bulk Photovoltaic Effect and Spontaneous Polarization of Single-Layer Monochalcogenides. *Phys. Rev. Lett.* **2017**, *119*, No. 067402.

(8) Panday, S. R.; Barraza-Lopez, S.; Rangel, T.; Fregoso, B. M. Injection Current in Ferroelectric Group-IV Monochalcogenide Monolayers. *Phys. Rev. B* **2019**, *100*, No. 195305.

(9) Fei, R.; Song, W.; Yang, L. Giant Photogalvanic Effect and Second-Harmonic Generation in Magnetic Axion Insulators. *Phys. Rev. B* **2020**, *102*, No. 035440.

(10) Wang, H.; Qian, X. Electrically and Magnetically Switchable Nonlinear Photocurrent in PT-Symmetric Magnetic Topological Quantum Materials. *NPJ Comput. Mater.* **2020**, *6*, na.

(11) Wang, H.; Qian, X. Ferroicity-Driven Nonlinear Photocurrent Switching in Time-Reversal Invariant Ferroic Materials. *Sci. Adv.* **2019**, *5*, na.

(12) Bhalla, P.; Das, K.; Culcer, D.; Agarwal, A. Resonant Second-Harmonic Generation as a Probe of Quantum Geometry. *Phys. Rev. Lett.* **2022**, *129*, No. 227401.

(13) Zhang, C.; Guo, P.; Zhou, J. Tailoring Bulk Photovoltaic Effects in Magnetic Sliding Ferroelectric Materials. *Nano Lett.* **2022**, *22*, 9297.

(14) Zhang, Y.; Holder, T.; Ishizuka, H.; de Juan, F.; Nagaosa, N.; Felser, C.; Yan, B. Switchable Magnetic Bulk Photovoltaic Effect in the Two-Dimensional Magnet CrI3. *Nat. Commun.* **2019**, *10*, 3783.

(15) Xue, Q.; Mu, X.; Sun, Y.; Zhou, J. Valley Contrasting Bulk Photovoltaic Effect in a PTY-Symmetric $MnPSe_3$ Monolayer. *Phys. Rev. B* **2023**, *107*, No. 245404.

(16) Wang, H.; Qian, X. Ferroelectric Nonlinear Anomalous Hall Effect in Few-Layer WTe2. *NPJ. Comput. Mater.* **2019**, *5*, 119.

(17) de Juan, F.; Grushin, A. G.; Morimoto, T.; Moore, J. E. Quantized Circular Photogalvanic Effect in Weyl Semimetals. *Nat. Commun.* **2017**, *8*, No. 15995.

(18) Xu, H.; Wang, H.; Zhou, J.; Li, J. Pure Spin Photocurrent in Non-Centrosymmetric Crystals: Bulk Spin Photovoltaic Effect. *Nat. Commun.* **2021**, *12*, na.

(19) Fei, R.; Song, W.; Pusey-Nazzaro, L.; Yang, L. PT-Symmetry-Enabled Spin Circular Photogalvanic Effect in Antiferromagnetic Insulators. *Phys. Rev. Lett.* **2021**, *127*, No. 207402.

(20) Fei, R.; Yu, S.; Lu, Y.; Zhu, L.; Yang, L. Switchable Enhanced Spin Photocurrent in Rashba and Cubic Dresselhaus Ferroelectric Semiconductors. *Nano Lett.* **2021**, *21*, 2265.

(21) Song, T. Spin Photovoltaic Effect in Magnetic van Der Waals Heterostructures. *Sci. Adv.* **2021**, *7*, na.

(22) Hamamoto, K.; Ezawa, M.; Kim, K. W.; Morimoto, T.; Nagaosa, N. Nonlinear Spin Current Generation in Noncentrosymmetric Spin-Orbit Coupled Systems. *Phys. Rev. B* **2017**, *95*, No. 224430.

(23) Lihm, J.-M.; Park, C.-H. Comprehensive Theory of Second-Order Spin Photocurrents. *Phys. Rev. B* **2022**, *105*, No. 045201.

(24) Ahn, J.; Guo, G.-Y.; Nagaosa, N. Low-Frequency Divergence and Quantum Geometry of the Bulk Photovoltaic Effect in Topological Semimetals. *Phys. Rev. X* **2020**, *10*, No. 041041.
(25) Ma, J.; Gu, Q.; Liu, Y.; Lai, J.; Yu, P.; Zhuo, X.; Liu, Z.; Chen, J.-H.; Feng, J.; Sun, D. Nonlinear Photoresponse of Type-II Weyl Semimetals. *Nat. Mater.* **2019**, *18*, 476.
(26) Rostami, H.; Polini, M. Nonlinear Anomalous Photocurrents in Weyl Semimetals. *Phys. Rev. B* **2018**, *97*, No. 195151.
(27) Steiner, J. F.; Andreev, A. V.; Breitkreiz, M. Surface Photogalvanic Effect in Weyl Semimetals. *Phys. Rev. Res.* **2022**, *4*, No. 023021.
(28) Chan, C.-K.; Lindner, N. H.; Refael, G.; Lee, P. A. Photocurrents in Weyl Semimetals. *Phys. Rev. B* **2017**, *95*, No. 041104.
(29) Taguchi, K.; Imaeda, T.; Sato, M.; Tanaka, Y. Photovoltaic Chiral Magnetic Effect in Weyl Semimetals. *Phys. Rev. B* **2016**, *93*, No. 201202.
(30) Osterhoudt, G. B.; et al. Colossal Mid-Infrared Bulk Photovoltaic Effect in a Type-I Weyl Semimetal. *Nat. Mater.* **2019**, *18*, 471.
(31) Holder, T.; Kaplan, D.; Yan, B. Consequences of Time-Reversal-Symmetry Breaking in the Light-Matter Interaction: Berry Curvature, Quantum Metric, and Diabatic Motion. *Phys. Rev. Res.* **2020**, *2*, No. 033100.
(32) Morimoto, T.; Nagaosa, N. Topological Nature of Nonlinear Optical Effects in Solids. *Sci. Adv.* **2016**, *2*, na.
(33) Gao, W.; Zhao, J.; Chelikowsky, J. R. Out-of-Plane Polarization and Topological Magnetic Vortices in Multiferroic $CrPSe_3$. *Phys. Rev. Mater.* **2022**, *6*, No. L101402.
(34) Zhang, J.-J.; Lin, L.; Zhang, Y.; Wu, M.; Yakobson, B. I.; Dong, S. Type-II Multiferroic Hf_2VC_2 F $_2$ MXene Monolayer with High Transition Temperature. *J. Am. Chem. Soc.* **2018**, *140*, 9768.
(35) Xu, M.; Huang, C.; Li, Y.; Liu, S.; Zhong, X.; Jena, P.; Kan, E.; Wang, Y. Electrical Control of Magnetic Phase Transition in a Type-I Multiferroic Double-Metal Trihalide Monolayer. *Phys. Rev. Lett.* **2020**, *124*, No. 067602.
(36) Liu, X.; Pyatakov, A. P.; Ren, W. Magnetoelectric Coupling in Multiferroic Bilayer VS_2. *Phys. Rev. Lett.* **2020**, *125*, No. 247601.
(37) Qi, J.; Wang, H.; Chen, X.; Qian, X. Two-Dimensional Multiferroic Semiconductors with Coexisting Ferroelectricity and Ferromagnetism. *Appl. Phys. Lett.* **2018**, *113*, na.
(38) Sun, Z.; et al. Observation of Topological Flat Bands in the Kagome Semiconductor Nb_3Cl_8. *Nano Lett.* **2022**, *22*, 4596.
(39) Peng, R.; Ma, Y.; Xu, X.; He, Z.; Huang, B.; Dai, Y. Intrinsic Anomalous Valley Hall Effect in Single-Nb_3I_8. *Phys. Rev. B* **2020**, *102*, No. 035412.
(40) Gao, S.; et al. Discovery of a Single-Band Mott Insulator in a van Der Waals Flat-Band Compound. *Phys. Rev. X* **2023**, *13*, No. 041049.
(41) Li, Y.; Liu, C.; Zhao, G.-D.; Hu, T.; Ren, W. Two-Dimensional Multiferroics in a Breathing Kagome Lattice. *Phys. Rev. B* **2021**, *104*, No. L060405.
(42) Feng, Y.; Yang, Q. Enabling Triferroics Coupling in Breathing Kagome Lattice Nb_3X_8 (X = Cl, Br, I) Monolayers. *J. Mater. Chem. C Mater.* **2023**, *11*, 5762.
(43) Regmi, S.; et al. Observation of Flat and Weakly Dispersing Bands in the van Der Waals Semiconductor Nb_3I_8 with Breathing Kagome Lattice. *Phys. Rev. B* **2023**, *108*, No. L121404.
(44) Regmi, S.; et al. Spectroscopic Evidence of Flat Bands in Breathing Kagome Semiconductor Nb3I8. *Commun. Mater.* **2022**, *3*, 100.
(45) Ahn, J.; Guo, G.-Y.; Nagaosa, N.; Vishwanath, A. Riemannian Geometry of Resonant Optical Responses. *Nat. Phys.* **2022**, *18*, 290.
(46) Wang, C.; Gao, Y.; Xiao, D. Intrinsic Nonlinear Hall Effect in Antiferromagnetic Tetragonal CuMnAs. *Phys. Rev. Lett.* **2021**, *127*, No. 277201.
(47) Jiang, J.; Liang, Q.; Meng, R.; Yang, Q.; Tan, C.; Sun, X.; Chen, X. Exploration of New Ferromagnetic, Semiconducting and Biocompatible Nb_3X_8 (X = Cl, Br or I) Monolayers with Considerable Visible and Infrared Light Absorption. *Nanoscale* **2017**, *9*, 2992.
(48) Schankler, A. M.; Gao, L.; Rappe, A. M. Large Bulk Piezophotovoltaic Effect of Monolayer 2H-MoS_2. *J. Phys. Chem. Lett.* **2021**, *12* (4), 1244.
(49) Spataru, C. D.; Ismail-Beigi, S.; Capaz, R. B.; Louie, S. G. Quasiparticle and Excitonic Effects in the Optical Response of Nanotubes and Nanoribbons. *Topics in Applied Physics*; Springer, 2007; pp 195−227.
(50) Arzate, N.; Mendoza, B. S.; Vázquez-Nava, R. A.; Ibarra-Borja, Z.; Álvarez-Núñez, M. I. Optical Spin Injection in MoS_2 Monolayers. *Phys. Rev. B* **2016**, *93*, No. 115433.
(51) Grytsiuk, S.; Katsnelson, M. I.; van Loon, E. G. C. P.; Rösner, M. Nb3Cl8: A Prototypical Layered Mott-Hubbard Insulator. *NPJ. Quantum Mater.* **2024**, *9*, 8.
(52) Murakami, Y.; Eckstein, M.; Werner, P. High-Harmonic Generation in Mott Insulators. *Phys. Rev. Lett.* **2018**, *121*, No. 057405.
(53) Murakami, Y.; Werner, P. Nonequilibrium Steady States of Electric Field Driven Mott Insulators. *Phys. Rev. B* **2018**, *98*, No. 075102.
(54) Conte, F.; Ninno, D.; Cantele, G. Layer-dependent electronic and magnetic properties of Nb_3I_8. *Phys. Rev. B Res.* **2020**, *2*, No. 033001.
(55) Chang, Y. T.; Chan, Y. H. Diagrammatic approach to excitonic effects on nonlinear optical response. *Phys. Rev. B* **2024**, *109*, No. 155437.

https://doi.org/10.1021/acs.jpclett.4c01844
J. Phys. Chem. Lett. 2024, 15, 8689−8696